Research Article
Vol. 16, No. 11 / 1 Nov 2025 / *Biomedical Optics Express* 4273

Biomedical Optics EXPRESS

Lightweight CNN efficiently discriminates ovarian cancer cells from a tumor microenvironment via holographic imaging flow cytometry

DANIELE PIRONE,[1,*] BEATRICE CAVINA,[2,3] GIUSY GIUGLIANO,[1,4] MICHELA SCHIAVO,[1,4,5,6] LISA MICCIO,[1] VITTORIO BIANCO,[1] FRANCESCA NANETTI,[2,3] FRANCESCA REGGIANI,[7] GIUSEPPE GASPARRE,[2,3] IVANA KURELAC,[2,3] PIETRO FERRARO,[1] AND PASQUALE MEMMOLO[1]

[1] *CNR-ISASI, Institute of Applied Sciences and Intelligent Systems "Eduardo Caianiello", Via Campi Flegrei 34, 80078 Pozzuoli (Napoli), Italy*
[2] *DIMEC, Department of Medical and Surgical Sciences, Alma Mater Studiorum-University of Bologna, 40138 Bologna, Italy*
[3] *Centre for Applied Biomedical Research (CRBA), University of Bologna, Bologna, Italy*
[4] *Department of Mathematics and Physics, University of Campania "Luigi Vanvitelli", Viale Abramo Lincoln 5, 81100 Caserta, Italy*
[5] *TIGEM, Telethon Institute of Genetics and Medicine, Via Campi Flegrei 34, 80078 Pozzuoli, Napoli, Italy*
[6] *Department of Advanced Biomedical Science, University of Naples "Federico II", Via Sergio Pansini 5, 80131 Napoli, Italy*
[7] *Translational Research Laboratory, Azienda Unità Sanitaria Locale-IRCCS di Reggio Emilia, viale Risorgimento 80, 42123 Reggio Emilia, Italy*
[*] *daniele.pirone@isasi.cnr.it*

Abstract: Holographic imaging flow cytometry (HIFC) can generate 2D quantitative phase maps of flowing cells in microchannels. When combined with convolutional neural networks (CNNs), HIFC could provide a promising stain-free approach for identifying target cells in complex cellular environments by leveraging the distinctive morphological and optical properties of different cell types. Here, we propose a lightweight CNN for HIFC image classification, tailored to distinguish ovarian cancer cells from surrounding non-neoplastic cell populations of the tumor microenvironment (TME). We show that the proposed CNN outperforms commonly used models, i.e., Resnet and VGG, with a computational cost lower than Mobilenet, the benchmark for efficiency and accuracy. Our approach could streamline ovarian cancer diagnostics and improve understanding of the TME, ultimately aiding the development of personalized treatments.

1. Introduction

Tumors are complex and heterogeneous ecosystems in which neoplastic cells and diverse non-malignant cells of the tumor microenvironment (TME) interact with one another, thus critically impacting disease progression, metastasis and response to treatment [1]. Therefore, optimizing methodological approaches able to understand and modulate the TME is one of the major goals in cancer biology [2]. In particular, visualization and characterization of the cellular heterogeneity and spatial architecture of the TME is becoming increasingly important to understand the pathological mechanisms of transformation, dissemination and chemoresistance onset [3,4]. TME most often includes lymphocytes (T- and B-cells), natural killer (NK) cells, tumor-associated macrophages (TAMs), myeloid-derived suppressor cells (MDSCs), mast cells, granulocytes, dendritic cells (DCs), tumor-associated neutrophils, cancer-associated fibroblasts

#545251
Journal © 2025
https://doi.org/10.1364/BOE.545251
Received 16 Oct 2024; revised 11 Dec 2024; accepted 11 Dec 2024; published 3 Oct 2025

(CAFs), adipocytes, vascular endothelial cells, pericytes and parenchymal cells of the tissue in which the cancer arises [4].

Recent studies have demonstrated that artificial intelligence (AI), combined with microscopy imaging, offers potential breakthrough solutions in TME understanding at single-cell level [5]. One prominent approach involves convolutional neural networks (CNNs) applied to 3D confocal imaging of single cells allowing the investigation of dynamic interactions between cancer cells and other TME components [6]. For example, advancements have been reached for brain TME classification of both tissue microarrays and segmented single cells within the tissue [7].

Recently, AI-powered label-free microscopy also enabled advanced TME understanding [8]. However, to date and to the best of our knowledge, quantitative phase imaging (QPI) methods have not yet been employed in this field. QPI is a label-free optical microscopy technique that offers the unique possibility of imaging and measuring biological specimens without the need for staining [9]. Undesired effects such as photobleaching and phototoxicity typical of well-established fluorescence microscopy may be indeed avoided, as well as the dependence of the result on the sample preparation protocol and the operator's expertise. In addition, QPI provides a quantitative assessment of the biophysical properties of the imaged sample. Therefore, QPI has undergone rapid development in recent decades, and several imaging techniques have been proposed to implement it, such as digital holography (DH) [10]. The advent of AI constituted a further turning point in the development of QPI techniques and their applications in biomedicine [11]. In this latter scenario, imaging flow cytometry has proved a valid solution for feeding the hunger of data typical of AI in single-cell classification problems [12]. Hence, holographic imaging flow cytometry (HIFC) combined with AI has been exploited for several purposes, mainly including the detection and phenotyping of cancer cells belonging to different tumor types, such as melanoma and colorectal adenocarcinoma [13,14], breast cancer [15], urothelial cancer [16], neuroblastoma [17,18], or ovarian cancer (OC) [18,19,20].

In this paper we focus on OC cells discrimination from a subset of related TME cell populations by using HIFC and CNN. It has been shown that appropriate analysis of OC TME, in terms of evaluating its content as well as defining malignant vs. immune cell quantitative ratio and spatial relationship, may predict survival and potentially aid calibrating personalized therapies [21,22]. Here we propose a lightweight but accurate CNN, termed TMEnet, for the classification of 2D QPMs of five cell populations, i.e. OC cells and four models of non-cancerous populations, namely lymphocytes, monocytes, NK and endothelial cells. TMEnet is compared with the most used state-of-the-art CNNs, namely Resnet50 [23] and VGG19 [24], commonly recognized as very accurate classification models, and with Mobilenets [25], usually acknowledged as the reference CNN model to balance lightness and accuracy. TMEnet shows superior performance with respect to Resnet50 and VGG19 models along with a computational burden lower than the Mobilenetv2. In particular, we demonstrate an overall accuracy of over 90%, attributable to improved predictions across all classes compared to the other models. Moreover, the proposed architecture reduces the number of learnable parameters by almost 70% with respect to MobileNetV2, making it highly suitable for deployment on mobile devices [26]. In addition, we perform independent experiments to acquire new OC cells with the aim of evaluating external generalization performance of our CNN in OC cell identification and quantification. The results demonstrate high identification rate (>95%), also in this case superior to the predictions made by Resnet50, VGG19 and Mobilenetv2, thus confirming the robustness of TMEnet.

2. Methods

2.1. Sample preparation

Human OC cell line CAOV3 was purchased from ATCC (#HB-75). Natural killer NK92 cell line was purchased from ATCC (#CRL-2407). Umbilical Vein Endothelial, Pooled Donors (HUVEC) cells were purchased from Lonza (#CC-2519). Monocyte THP1 and JURKAT peripheral blood-derived human T-cell leukemia cell line were authenticated as previously described in [27].

CAOV3, THP1, and JURKAT cells were cultured in RPMI 1640 Medium (Euroclone #ECB9006) supplemented with 20% FBS South America origin EU Approved (Euroclone #ECS5000 L), 2 mM L-glutamine (Euroclone #ECB3000D), 1% penicillin/streptomycin (Euroclone #ECB3001D), the first cell line in adhesion, the latter two in suspension. NK92 cell line was maintained in suspension and grown in Mem-alpha medium without nucleosides (Thermo Fisher #12561056) + 12.5% FBS South America (Gibco #A5256701) + 12.5% Horse serum (Thermo Fisher #26050088) + 1.5 g/l Sodium Bicarbonate (Thermo Fisher #25080094) + 0.1 mM 2-mercapto-ethanol (Thermo Fisher #31350010) + 1% L-Glutamine (Eurclone #ECB3000D) + 1% penicillin/streptomycin (Euroclone #ECB3001D) + 0.02 mM Folic Acid (Sigma #I7508) + 0.2 mM Myo-inositol (Sigma #I7508); and freshly added with 200U/ml recombinant human IL-2 (Prepotech, #200-02) according to Manufacturer's instructions [28]. HUVEC cells were cultured in EBM-2 Basal Medium (#CC-3156) enriched with EGM-2 SingleQuots Supplements (#CC-4176) providing the necessary nutrients and signaling molecules for growth, provided by Lonza.

All cell lines were grown in an incubator at 37°C with a humidified atmosphere at 5% CO_2, regularly tested for mycoplasma, and passaged once 70-90% of confluence was reached. For sample preparation, NK92, THP1, and JURKAT cells were harvested, centrifuged for 5 min at 1500 rpm, washed with 10 mL PBS, and resuspended in their culture medium for the subsequential cell counting. CAOV3 and HUVEC cells were detached following standard procedure, meaning medium removal, PBS washing, and incubation with Trypsin-EDTA (Sigma #T8154) for 5 min at 37°C. Next, the cell culture medium was added for each cell line to block trypsin activity. Cells were counted using Burker Cell Counter and Trypan Blue dye (Sigma #T8154) for viability assessment. In detail, two independent counts were performed for each cell line by diluting 1:2 cell suspension with Trypan Blue, and 0.01 mL was loaded in the cell counter. The experimental cell suspension was prepared considering the average live cell count, and each cell line was diluted in its culture medium to 2×10^5 cells/mL of which 200µL were injected into the microfluidic channel.

2.2. HIFC experimental system

To perform holographic recording of flowing cells, we implemented a DH microscope employing a Mach Zehnder interferometer based on off-axis configuration, as sketched in Fig. 1(a) [27]. The interference fringe pattern is achieved by means of a Beam Splitter cube (BS) that recombines object and reference beams. The two beams are obtained after splitting a light wave generated by a laser (Laser Quantum Torus 532, beam diameter 1.7 ± 0.2 mm) using a Polarizing Beam Splitter (PBS). Two Half-Wave Plates (HWPs) are placed in front of and behind the PBS for balancing the intensities of the two beams without changing their polarization. The object beam illuminates the cells while they roto-translate in the Microfluidic Channel (MC, Microfluidic ChipShop 10 000 107 – 200µm × 1000µm × 58.5 mm). The scattered portion of the object beam is collected by a Microscope Objective (MO1, Zeiss Plan-Apochromat 40×, NA = 1.3, oil immersion) and passes through a Tube Lens (L1). At the same time, the reference beam passes through a Beam Expander (BE), which consists of a second Microscope Objective (MO2), a second Tube Lens (L2), and a Pinhole. The resulting hologram is recorded by a CMOS camera (Genie Nano-CXP Cameras – 5120 × 5120 pixels, 4.5µm pixel) at a frame rate of 30 Hz and an exposure time of 50µs. Cells are injected into the MC using an automatic syringe pump (CETONI Syringe Pump neMESYS 290N) that allows dosing sample injections at 75nl/s. As laminar flow is generated within the MC, in addition to the cells' flow, their rotation is induced by taking advantage of the hydrodynamic forces. Let xyz be the coordinate reference system, cells flow along the y-axis, rotate around the x-axis, and are imaged along the optical z-axis.

Hence, the CMOS camera records the holographic video sequence of the cells' roto-translation [27]. An example of 5120 × 5120 digital hologram recorded by the HIFC system is shown in Fig. 1(b). It is important to note that no blur occurs during holographic recording because the cell velocity is very low compared to the exposure time. Indeed, on average, each cell has a velocity of ~120μm/s, meaning that a cell covers about 6 nm during the exposure time. However, this distance is much smaller than the pixel size, which is 125 nm (i.e., only 4.8%).

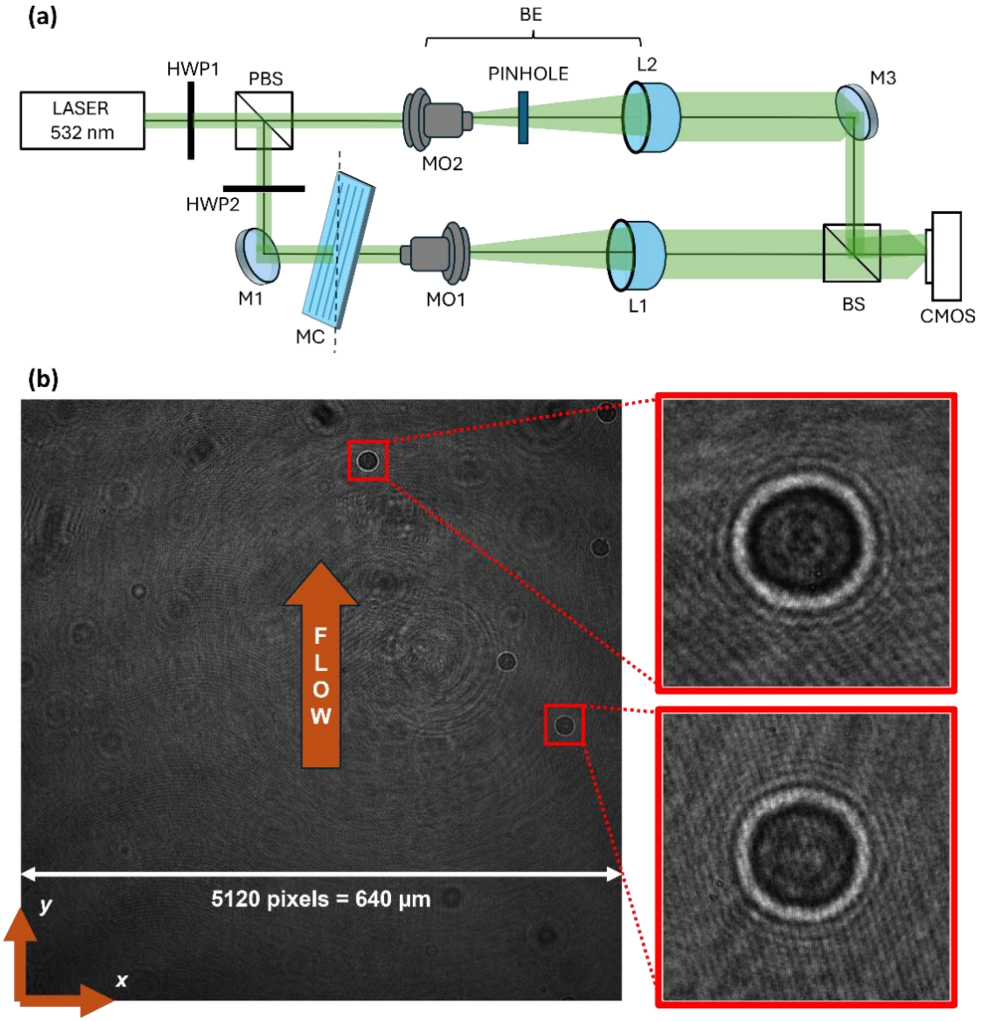

Fig. 1. HIFC experiments. (a) DH microscope in off-axis configuration. HWP, half-wave plate; PBS, polarizing beam splitter; L, tube lens; M, mirror; MO, microscope objective; MC, microfluidic channel; BS, beam splitter; CMOS, camera. (b) Digital hologram recorded by the HIFC system, with zoomed-in the holographic ROIs containing CAOV3 cells. Cells flow along the y-axis, rotate around the x-axis, and are imaged along the optical z-axis.

2.3. HIFC numerical reconstruction

Cells are detected and tracked from the holographic video sequence recorded by the HIFC system. In each frame, a region of interest (ROI) is selected around each detected cell, as displayed in Fig. 1(b). Therefore, the holographic video sequence is converted into multiple sequences of holographic ROIs, each of which contains the roto-translation of a specific cell. A quantitative phase map (QPM) is then computed from each holographic ROI. By applying a band-pass filtering in the Fourier domain, the real diffraction order is numerically isolated, thus obtaining the demodulated hologram [29]. Through the minimization of the Tamura coefficient, the proper focus distance is evaluated in order to achieve the numerical refocusing of the holographic ROI by propagating the complex field at such distance [30]. The phase contrast image is extracted from the refocused complex wavefront, and after compensation of aberrations by subtraction of a reference hologram [31], the phase denoising [32] and phase unwrapping [33] are performed to retrieve the 101 × 101 QPM.

2.4. Proposed CNN model

In order to discriminate OC cells from a subset of related TME cell populations, we created a custom-made CNN, termed here TMEnet. TMEnet is a VGGnet style architecture [24] inspired by the CNN proposed in [34] for image homography estimation. Such network uses 8 convolutional layers (3 × 3), each followed by a batch normalization and ReLU activation, and a max pooling layer (2 × 2, stride 2) after every two convolutions. The first 4 convolutional layers employ 64 filters while the last 4 convolutional layers use 128 filters. Each convolutional layer has a default setting of hyperparameter except for the output padding that is fixed to have the same size of the input. Batch normalization is also used with the default parameters setting. The convolutional blocks are followed by a fully connected layer having 1024 units, a ReLU activation layer, and a dropout with a probability of 0.5. Next, a second fully connected layer is set to the number of classes, and a softmax layer is employed for classification, optimizing weights using cross-entropy as the loss function. This architecture has been demonstrated to be highly efficient in the homography regression task but requires optimizing 9 million learnable parameters. By adapting this network to our classification problem, i.e. using as input the QPM sized 101 × 101 and considering 5 classes, we reduced the learnables to 5.3 million. However, the network complexity is still high to be considered light, so we took inspiration from Resnet models [23] in which fully connected layers are replaced by convolutional layers. Therefore, the proposed TMEnet shares the same architecture of the model in [34], but we employed the combination of a convolutional layer with unitary sized kernel and 1024 filters, as well as a global max pooling layer in place of the fully connected layer. This modification drastically reduces the learnables to 0.77 million with a corresponding memory occupation of less than 3MB after training. A sketch of the TMEnet is reported in Fig. 2.

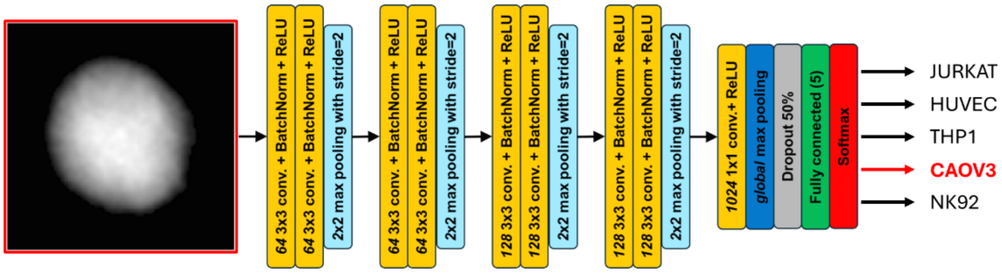

Fig. 2. TMEnet architecture.

The training step was performed over 50 epochs with a batch size of 64 (116 iterations per epoch), with a stopping criterion based on the best validation loss. We used the ADAM optimizer with a learning rate of 10^{-3}, reduced by a further 0.1 drop factor for the last 5 epochs. Training was performed in the Matlab R2023b environment over a laptop equipped with a 12th Gen Intel Core i9-12900HK 2.50 GHz, 64 GB RAM, and a NVIDIA GeForce RTX 3050 Ti Laptop GPU.

3. Results

To train and test a CNN for distinguishing OC cells from other TME subpopulations, a dataset of 2D QPMs was collected by using the HIFC system. According to Table 1, the entire set was composed of 1635 cells, including THP1 (i.e., monocytes), JURKAT (i.e., lymphocytes), NK92 (i.e., NKs), HUVEC (i.e., endothelial cells), and CAOV3 (i.e., OC cells). Due to the roto-translation of single cells along the microfluidic channel of the HIFC system employed, multiple QPMs per cell were acquired containing different views of the same biological sample. Cells flow about at the same speed, depending on their exact height in the microfluidic channel. This means that almost the same number of QPMs was recorded for each cell. However, as reported in Table 1, different numbers of cells were collected during experiments for each cell line. In order to balance class sizes during training and testing, we selected different numbers of QPMs per cell for each specific cell line, thus also augmenting the observations. The numbers of selected QPMs for each cell line are summarized in Table 1. An example of a QPM is shown in Fig. 3 for each class. A QPM quantifies the phase delay introduced by the biological object on the incident wavefront [9,10,35]. Therefore, it contains information about cell morphology and is strictly related to its refractive index values. For this reason, quantitative measurements can be conducted on the biological sample, involving its morphological and biophysical features [36,37,38]. For example, to understand the QPI-based clustering of the cytotypes analyzed, we considered the two most typical QPI features, i.e. the cell area for morphological characterization and the cell dry mass density for biophysical characterization. In particular, the cell area was computed by summing up all the pixels within the binary cell mask, obtained automatically by the following threshold-based segmentation

Table 1. Dataset collected by the HIFC system for training a CNN

Cell Line	# Cells	# QPMs			
	Overall	Overall	Training	Validation	Test
THP1	635	1721	1549	86	86
JURKAT	1231	1534	1381	77	76
NK92	500	1730	1557	87	86
HUVEC	411	1621	1459	81	81
CAOV3	203	1686	1517	85	84
	2980		*8292*	*7463*	*416*

$$\text{mask}(x, y) = \{(x, y) \mid QPM(x, y) - \mu > 0.5\text{rad}\}, \tag{1}$$

where μ is the mean QPM value. Instead, the cell dry mass density can be defined as the cell mass without considering its water content, normalized to cell area, i.e.

$$m = \frac{\lambda}{2\pi\alpha} \sum\nolimits_{x,y} QPM(x, y), \tag{2}$$

where λ is the wavelength and α is the refractive increment, which can be set as 0.190 ml/g [9]. We compared the five cell lines according to these two features in the scatterplot of Fig. 3. By observing the univariate histograms containing the marginal distributions, it can be inferred that CAOV3 are the largest cells, followed by HUVEC, NK92, and THP1/JURKAT cells. Instead, in terms of dry mass density, HUVEC, NK92, THP1, and JURKAT cells have mostly overlapping phenotypes, while CAOV3 cells are densest. Hence, in the scatterplot of Fig. 3, a CAOV3 cell cluster may be appreciated, partially distinguishable from the other cell types. However, it shares a non-negligible overlap region, which is why we implemented a CNN to extract suitable features able to maximize cluster separation, leading to high classification performance in distinguishing CAOV3 cells within the TME.

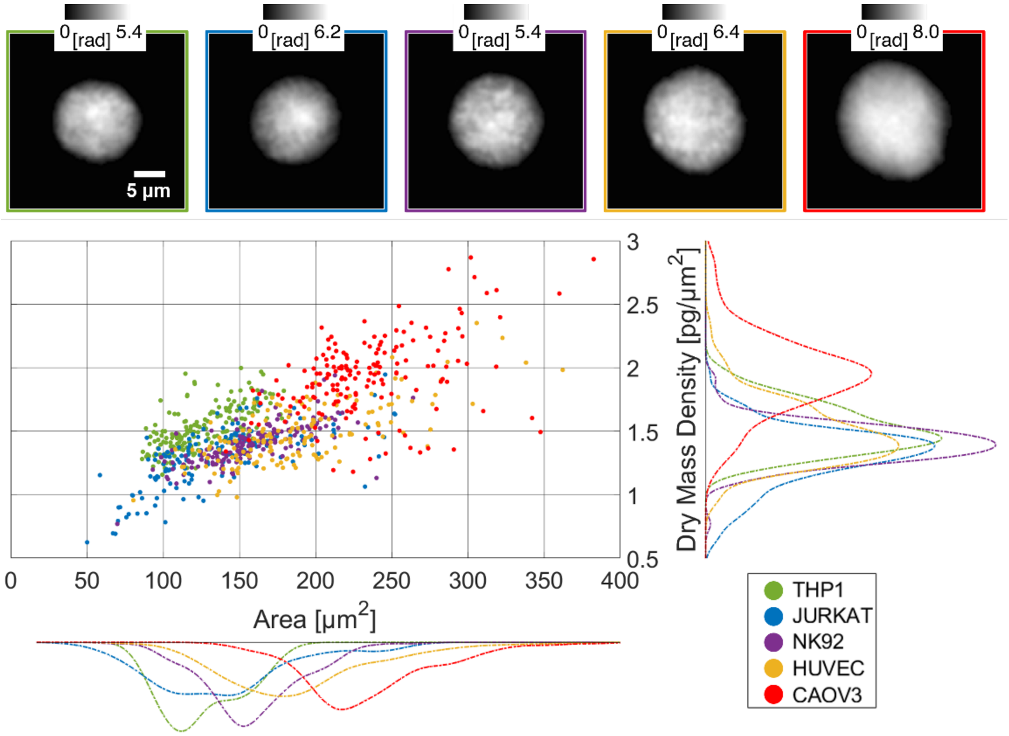

Fig. 3. Visual inspection of the HIFC dataset. At the top, an example of 2D QPM for each of the cell lines analyzed; at the bottom, scatterplot of the cell area vs. the cell dry mass density computed from the 2D QPMs, along with the univariate histograms containing the corresponding marginal distributions and reporting the frequency of occurrences of the represented feature.

In order to assess the effectiveness of the TMEnet, we compared its performance with three state-of-the-art CNN models, i.e. the Resnet50 [23] and the VGG19 [24], recognized as high-performance networks for image classification, and the Mobilenetv2 [25], usually considered the reference lightweight CNN model. For a balanced comparison, all CNNs were trained with the same datasets and training options described in the Methods. In particular, the training set had 7463 QPMs obtained by randomly extracting 90% of images from each class of the overall dataset (see Table 1). To assess the performance of the trained TMEnet, we employed a test set composed of the remaining 5% of QPMs inside the overall dataset (i.e., 413 images different from those used for training and validation, see Table 1). The classification performances of the TMEnet are shown in Fig. 4 (see also the corresponding confusion matrices in the Supplement 1), averaged among three different trainings of the network carried out to consider statistical variability. Specifically, given a certain class, we employed the recall and the F1 score as classification metrics [39]. The recall of a certain class is defined as the percentage of QPMs correctly classified as that class with respect to the total number of QPMs within that class. The F1 score is the harmonic mean between recall and precision, where the precision of a certain class is defined as the percentage of QPMs correctly classified as that class with respect to the total number of QPMs assigned to that class. Hence, given the QPM of a certain class, the recall measures the probability of predicting its true class, while, given the prediction of a certain class, the precision

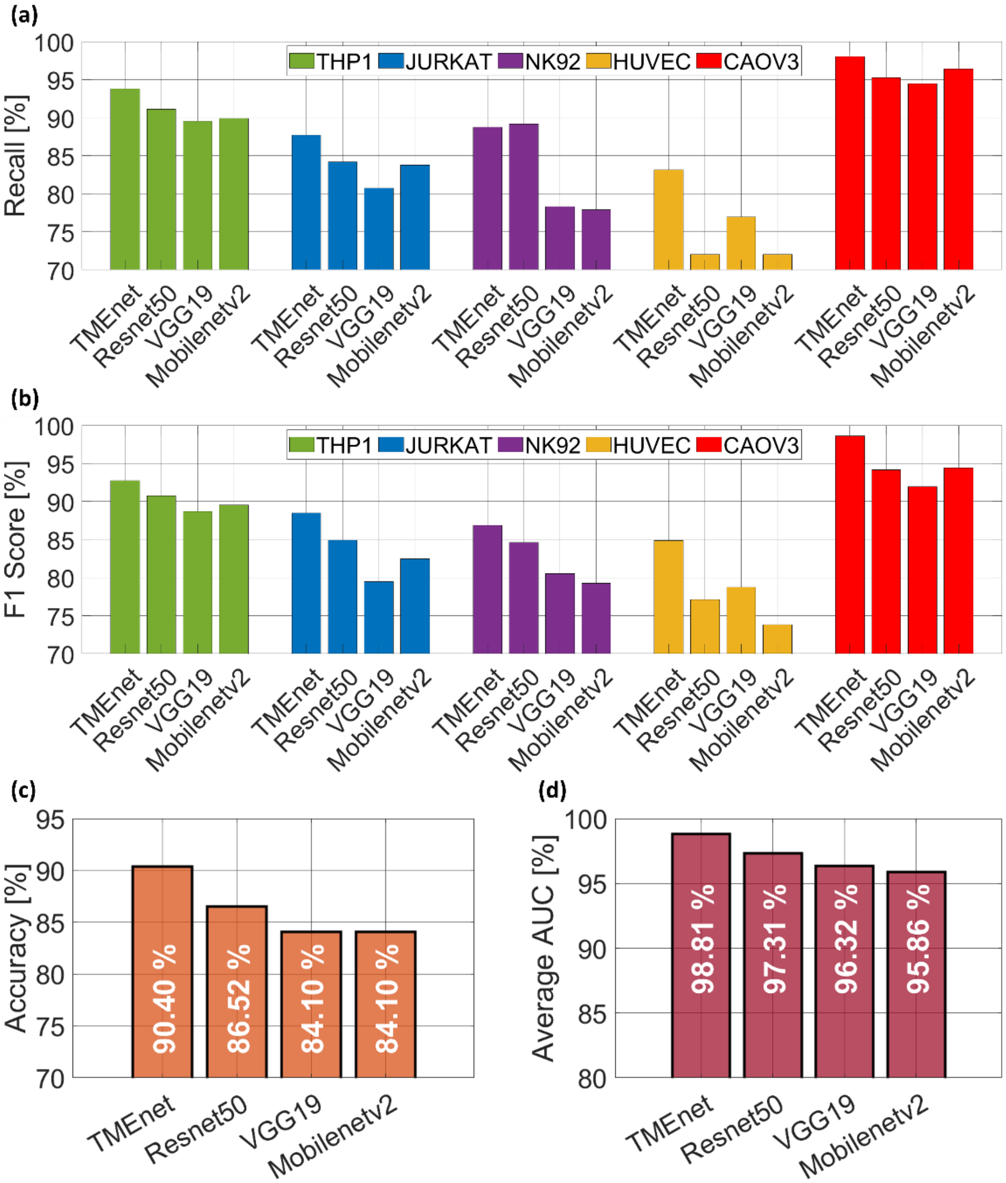

Fig. 4. Comparison among the classification metrics of different CNNs computed over the test set and averaged among three different trainings. (a) Recall of each cell line. (b) F1 score of each cell line. (c) Global accuracy. (d) Average AUC among the five cell lines.

measures the probability that it is correct. By observing Figs. 4(a,b), respectively, TMEnet was able to predict the THP1 class with a recall of 93.80% and an F1 score of 92.71%, the JURKAT class with a recall of 87.72% and an F1 score of 88.48%, the NK92 class with a recall of 88.76% and an F1 score of 86.89%, the HUVEC class with a recall of 83.13% and an F1 score of 84.87%, and the CAOV3 class with a recall of 98.02% and an F1 score of 98.60%. As expected by the quantitative analysis of Fig. 3, the best performance was obtained with the CAOV3 class. Instead, as global performance metrics of TMEnet, we employed accuracy and the area under curve (AUC) [39]. Accuracy is defined as the percentage of QPMs correctly classified with respect to the total number of images within the test set, and it can be interpreted as the probability of predicting the true class of any QPM. The AUC is instead defined as the average area under the five Receiver Operating Characteristic (ROC) curves, where the ROC curve of a certain class is the curve of the true positive rate (TPR) against the false positive rate (FPR) at different threshold settings. The TPR of a certain class corresponds to the recall and the FPR of a certain class corresponds to the percentage of QPMs wrongly predicted within that class with respect to the total images of the other classes (i.e., it is the probability that a QPM not belonging to a certain class is wrongly predicted as such). Hence, by observing Figs. 4(c,d), respectively, TMEnet reached an accuracy of 90.40% and an average AUC of 98.81% over the five classes of the test set.

Furthermore, a comparison among the four CNNs in terms of recall and F1 score is reported in Figs. 4(a,b), respectively, separated for each cell line. Generally, except for the NK92 recall (+0.39% increase of Resnet50 compared to TMEnet), TMEnet was the best model for all classes. Indeed, as global classification metrics, the best accuracy and the best AUC were reached by TMEnet, as shown in Figs. 4(c,d), respectively.

The objective of the proposed approach based on the CNN-based classification of HIFC images was the specific recognition of CAOV3 cells within an OC TME. For this reason, we carried out an additional experiment to collect an independent dataset of 179 CAOV3 cells. In this case, we acquired one single QPM per cell, thus emulating a much faster and simpler HIFC scenario in which all the hurdles to induce and record the cell rotation are avoided. For each CNN architecture, among the three trained models, we chose the one reaching the best recall over the internal test set. As summarized in Table 2, the highest recall for the CAOV3 class in the independent test set was reached by TMEnet (95.53%), followed by Mobilenetv2 and VGG19 (91.06%), and by Resnet50 (87.71%). Hence, TMEnet showed also the best ability of generalization over an experiment independent from the training one. Furthermore, when evaluating the performance of a CNN, the classification metrics are not the sole parameters to be taken into account, above all when the CNN is thought to be implemented for real-world applications. In this latter case, also technological parameters of the CNN must be considered, such as memory usage and deploy time (see Table 2). In particular, TMEnet had the fastest deploy time on a single QPM (2.7 ms), which is crucial for real-time applications, as well as the smallest memory usage (2.75MB), important for example for on-chip implementations, which were lower than the Mobilenetv2 (3.1 ms and 8.3MB) and much lower than the Resnet50 (6.2 ms and 86.6MB) and the VGG19 (10.9 ms and 195.0MB). A visual comparison among the four CNNs in terms of recall, deploy time, and memory usage is displayed in Fig. 5, in which it is clear that the best trade-off was provided by the TMEnet.

Table 2. Comparison among the properties of different CNN models

	TMEnet	Resnet50	VGG19	Mobilenetv2
# Layers	35	177	47	154
# Learnables [M]	0.77	23.5	55.7	2.2
Memory usage [MB]	2.75	86.6	195.0	8.3
Training time 50 epochs [min]	32	84	135	49
Deploy time [ms]	2.7	6.2	10.9	3.1
Average Accuracy Test [%]	90.40	86.52	84.10	84.10
Average Recall Test CAOV3 [%]	98.02	95.24	94.44	96.43
Recall Independent Test CAOV3 [%]	95.53	87.71	91.06	91.06

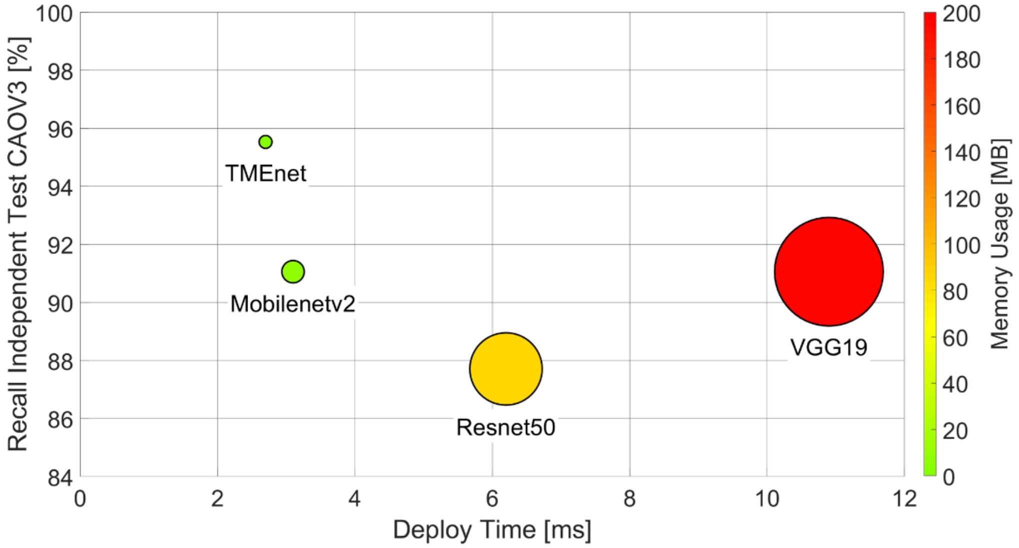

Fig. 5. Comparison among the recall, deploy time, and memory usage of different CNN models. The circle's radius is proportional to the memory usage of the corresponding CNN model.

4. Discussion and conclusions

Non-neoplastic cells within a tumor mass significantly contribute to tumor progression, playing an important role in defining disease outcome and often response to therapy [2,21,22], rendering them a significant biomarker. Implementing our understanding of TME from bench to bedside is one of the main current challenges in cancer research. In particular, to allow fast translation to the clinics, novel techniques should optimally be operator-independent and without requirements for highly specialized and trained personnel. In this context, we provide a proof-of-concept for the efficient discrimination of OC cells from several TME populations, the first step required for separation and appropriate quantification of both cancer and TME cells, exploiting for the first time the capabilities of HIFC combined with deep learning.

The proposed TMEnet has been demonstrated to be highly sensitive in detecting OC cells and related TME populations in comparison with the currently available state-of-the-art CNN models, such as Resnet [23] and VGG [24]. On the other hand, the use of mobile terminals is becoming more and more widespread. Therefore, in order to deploy CNNs to such EDGE devices for on-line monitoring, it is necessary to carry out lightweight architectures while preserving the overall model accuracy and robustness [26]. This objective has been achieved by TMEnet, as it provides an excellent trade-off among memory usage, deploy time, and classification accuracy, with a total computational burden lower than the Mobilenetv2 [25]. Specifically, we observed a remarkable improvement in terms of the most common performance metrics, as summarized in Fig. 4, Table 2, and in the Supplement 1, which reports some additional details about prediction errors. In general, by exploring the confusion matrices reported in Fig. S1, it is evident that HUVEC and NK92 populations are the most similar classes in terms of classification. In fact, it is possible to note that most of the prediction errors about the HUVEC class are due to a misclassification with the NK92 class, and vice versa. This is more evident for VGG19 and Mobilenetv2, while both Resnet50 and TMEnet provide higher comparable accuracies in predicting NK92, thus improving the overall performance. Noteworthy, the TMEnet outperforms all the other models in predicting all the other cell lines considered in this study. This is further confirmed by analyzing the prediction performance obtained for the independent experiment performed to collect new CAOV3 cells, in which the TMEnet allows higher sensitivity with respect to the other models, achieving an identification rate $> 95\%$.

However, we acknowledge the level of sample complexity in this pioneering study is relatively low, as we used only one cancer cell model, which does not account for the high intra- and inter-patient heterogeneity typically found in OC [40,41,21]. While it is well known that a high number of cell subtypes is typically present within any tumor mass, including neutrophils, adipocytes, fibroblasts, etc. [42], we preliminarily used four such cytotypes in this study. Notably, this included a TME population similar to cancer cells, specifically monocytes, which we represented using the THP1 model and successfully discriminated. Thus, we expect our method to be successful also in samples of higher complexity, which warrants further studies. Moreover, it is expected that the sample processing and the final buffer within which the cells are passed through the cytometer may affect their biophysical properties, which is why we suggest future studies should consider standardization of the protocols used for preanalytical steps.

In summary, even if the results reported here represent a proof-of-concept study, we believe that the proposed TMEnet has demonstrated remarkable generalization capabilities and robustness to be considered for a deeper TME analysis. In addition, the lightness of the proposed network architecture allows an important margin to design a deeper version of the TMEnet to match the definite increase of complexity expected in the challenging classification task of all TME populations.

Funding. Ministero dell'Università e della Ricerca (B53D23002280006).

Acknowledgment. This work was supported by project PRIN 2022, Computationally aided Opto-mechano-fluidic pLatform for Label-free intelligent tumor microEnvironment Cell sorTing (COLLECT) Prot. 202275PJRP, funded by the Italian Ministry of University & Research in the framework of the European Union program Next Generation EU, CUP: B53D23002280006. The project was also partly supported by Associazione Italiana per la Ricerca sul Cancro (AIRC) project IG 2019 - ID. 22921 to GG.

Disclosures. The authors declare no conflicts of interest.

Data availability. Data underlying the results presented in this paper are not publicly available at this time but may be obtained from the authors upon reasonable request.

Supplemental document. See Supplement 1 for supporting content.

References

1. S. Mayer, T. Milo, A. Isaacson, *et al.*, "The tumor microenvironment shows a hierarchy of cell-cell interactions dominated by fibroblasts," Nat. Commun. **14**(1), 5810 (2023).
2. M. Binnewies, E. W. Roberts, K. Kersten, *et al.*, "Understanding the tumor immune microenvironment (TIME) for effective therapy," Nat. Med. **24**(5), 541–550 (2018).
3. L. A. Walsh and D. F. Quail, "Decoding the tumor microenvironment with spatial technologies," Nat. Immunol. **24**(12), 1982–1993 (2023).
4. M. Z. Jin and W. L. Jin, "The updated landscape of tumor microenvironment and drug repurposing," Signal Transduct. Target. Ther. **5**(1), 166 (2020).
5. T. Xie, A. Huang, H. Yan, *et al.*, "Artificial intelligence: illuminating the depths of the tumor microenvironment," J. Transl. Med. **22**(1), 799 (2024).
6. B. Liu, Y. Zhu, Z. Yang, *et al.*, "Deep learning-based 3D single-cell imaging analysis pipeline enables quantification of cell-cell interaction dynamics in the tumor microenvironment," Cancer Res. **84**(4), 517–526 (2024).
7. M. Pytlarz, K. Wojnicki, P. Pilanc, *et al.*, "Deep learning glioma grading with the tumor microenvironment analysis protocol for comprehensive learning, discovering, and quantifying microenvironmental features," J. Imaging Inform. Med. **37**(4), 1711–1727 (2024).
8. S. You, E. J. Chaney, H. Tu, *et al.*, "Label-free deep profiling of the tumor microenvironment," Cancer Res. **81**(9), 2534–2544 (2021).
9. Y. Park, C. Depeursinge, and G. Popescu, "Quantitative phase imaging in biomedicine," Nat. Photon. **12**(10), 578–589 (2018).
10. V. Balasubramani, M. Kujawińska, C. Allier, *et al.*, "Roadmap on digital holography-based quantitative phase imaging," J. Imaging **7**(12), 252 (2021).
11. J. Park, B. Bai, D. Ryu, *et al.*, "Artificial intelligence-enabled quantitative phase imaging methods for life sciences," Nat. Methods **20**(11), 1645–1660 (2023).

12. S. Luo, Y. Shi, L. K. Chin, *et al.*, "Machine-learning-assisted intelligent imaging flow cytometry: A review," Adv. Intell. Syst. **3**(11), 2100073 (2021).
13. D. Roitshtain, L. Wolbromsky, E. Bal, *et al.*, "Quantitative phase microscopy spatial signatures of cancer cells," Cytometry, Part A **91**(5), 482–493 (2017).
14. N. Nissim, M. Dudaie, I. Barnea, *et al.*, "Real-time stain-free classification of cancer cells and blood cells using interferometric phase microscopy and machine learning," Cytometry, Part A **99**(5), 511–523 (2021).
15. A. Cohen, M. Dudaie, I. Barnea, *et al.*, "Label-free imaging flow cytometry for cell classification based on multiple interferometric projections using deep learning," Adv. Intell. Syst. **6**(1), 2300433 (2024).
16. L. Xin, X. Xiao, W. Xiao, *et al.*, "Screening for urothelial carcinoma cells in urine based on digital holographic flow cytometry through machine learning and deep learning methods," Lab Chip **24**(10), 2736–2746 (2024).
17. D. Pirone, A. Montella, D. Sirico, *et al.*, "Phenotyping neuroblastoma cells through intelligent scrutiny of stain-free biomarkers in holographic flow cytometry," APL Bioeng. **7**(3), 036118 (2023).
18. D. Pirone, A. Montella, D. G. Sirico, *et al.*, "Label-free liquid biopsy through the identification of tumor cells by machine learning-powered tomographic phase imaging flow cytometry," Sci. Rep. **13**(1), 6042 (2023).
19. D. Pirone, B. Cavina, D. G. Sirico, *et al.*, "Clinically informed intelligent classification of ovarian cancer cells by label-free holographic imaging flow cytometry," Adv. Intell. Syst. 2400390 (2024).
20. F. Borrelli, J. Behal, A. Cohen, *et al.*, "AI-aided holographic flow cytometry for label-free identification of ovarian cancer cells in the presence of unbalanced datasets," APL Bioeng **7**(2), 026110 (2023).
21. A. W. Zhang, A. McPherson, K. Milne, *et al.*, "Interfaces of malignant and immunologic clonal dynamics in ovarian cancer," Cell **173**(7), 1755–1769.e22 (2018).
22. C. Y. Yeh, K. Aguirre, O. Laveroni, *et al.*, "Mapping spatial organization and genetic cell-state regulators to target immune evasion in ovarian cancer," Nat. Immunol. **25**(10), 1943–1958 (2024).
23. K. He, X. Zhang, S. Ren, *et al.*, "Deep residual learning for image recognition," in *Proceedings of the IEEE conference on computer vision and pattern recognition* (2016), pp. 770–778.
24. K. Simonyan and A. Zisserman, "Very deep convolutional networks for large-scale image recognition," in *3rd International Conference on Learning Representations (ICLR)* (2015), pp. 1–14.
25. M. Sandler, A. Howard, M. Zhu, *et al.*, "Mobilenetv2: Inverted residuals and linear bottlenecks," in *Proceedings of the IEEE conference on computer vision and pattern recognition* (2018), pp. 4510–4520.
26. Y. Zhou, S. Chen, Y. Wang, *et al.*, "Review of research on lightweight convolutional neural networks," In *2020 IEEE 5th Information Technology and Mechatronics Engineering Conference (ITOEC)* (2020), pp. 1713–1720.
27. D. Pirone, G. La Verde, J. Behal, *et al.*, "Estimating the effects of x-ray radiations on lymphocytes by minimally invasive holographic imaging flow cytometry," J. Phys. D: Appl. Phys. **57**(50), 505402 (2024).
28. J. H. Gong, G. Maki, and H. G. Klingemann, "Characterization of a human cell line (NK-92) with phenotypical and functional characteristics of activated natural killer cells," Leukemia **8**(4), 652–658 (1994).
29. G. Dwivedi, S. K. Debnath, B. Das, *et al.*, "Revisit to comparison of numerical reconstruction of digital holograms using angular spectrum method and Fresnel diffraction method," J. Opt. **49**(1), 118–126 (2020).
30. P. Memmolo, C. Distante, M. Paturzo, *et al.*, "Automatic focusing in digital holography and its application to stretched holograms," Opt. Lett. **36**(10), 1945–1947 (2011).
31. C. Trujillo, R. Castañeda, P. Piedrahita-Quintero, *et al.*, "Automatic full compensation of quantitative phase imaging in off-axis digital holographic microscopy," Appl. Opt. **55**(36), 10299–10306 (2016).
32. Q. Kemao, H. Wang, and W. Gao, "Windowed Fourier transform for fringe pattern analysis: theoretical analyses," Appl. Opt. **47**(29), 5408–5419 (2008).
33. J. M. Bioucas-Dias and G. Valadao, "Phase unwrapping via graph cuts," IEEE Trans. on Image Process. **16**(3), 698–709 (2007).
34. D. DeTone, T. Malisiewicz, and A. Rabinovich, "Deep image homography estimation," arXiv (2016).
35. M. K. Kim, "Principles and techniques of digital holographic microscopy," SPIE Reviews **1**(1), 018005 (2010).
36. J. Min, B. Yao, V. Trendafilova, *et al.*, "Quantitative phase imaging of cells in a flow cytometry arrangement utilizing Michelson interferometer-based off-axis digital holographic microscopy," J. Biophotonics **12**(9), e201900085 (2019).
37. G. O. Dwapanyin, D. J. Chow, T. C. Tan, *et al.*, "Investigation of refractive index dynamics during in vitro embryo development using off-axis digital holographic microscopy," Biomed. Opt. Express **14**(7), 3327–3342 (2023).
38. K. C. Lee, M. Wang, K. S. Cheah, *et al.*, "Quantitative phase imaging flow cytometry for ultra-large-scale single-cell biophysical phenotyping," Cytometry, Part A **95**(5), 510–520 (2019).
39. A. Tharwat, "Classification assessment methods," Appl. Comput. Inform. **17**(1), 168–192 (2021).
40. R. F. Schwarz, C. K. Ng, S. L. Cooke, *et al.*, "Spatial and temporal heterogeneity in high-grade serous ovarian cancer: a phylogenetic analysis," PLoS Med. **12**(2), e1001789 (2015).
41. P. Smith, T. Bradley, L. M. Gavarró, *et al.*, "The copy number and mutational landscape of recurrent ovarian high-grade serous carcinoma," Nat. Commun. **14**(1), 4387 (2023).
42. Q. Zhao, H. Shao, and T. Zhang, "Single-cell RNA sequencing in ovarian cancer: revealing new perspectives in the tumor microenvironment," Am. J. Transl. Res **16**(7), 3338–3354 (2024).